

Phase separation of a repulsive two-component Fermi gas at the two- to three-dimensional crossover

Piotr T. Grochowski ^{1,2,3,*}, Martin-Isbjörn Trappe ⁴, Tomasz Karpiuk,⁵ and Kazimierz Rzażewski ³

¹*Institute for Quantum Optics and Quantum Information of the Austrian Academy of Sciences, A-6020 Innsbruck, Austria*

²*Institute for Theoretical Physics, University of Innsbruck, A-6020 Innsbruck, Austria*

³*Center for Theoretical Physics, Polish Academy of Sciences, Aleja Lotników 32/46, 02-668 Warsaw, Poland*

⁴*Centre for Quantum Technologies, National University of Singapore, 3 Science Drive 2, Singapore 117543, Singapore*

⁵*Wydział Fizyki, Uniwersytet w Białymstoku, Ulica K. Ciołkowskiego 1L, 15-245 Białystok, Poland*



(Received 15 November 2023; revised 10 July 2024; accepted 9 August 2024; published 27 August 2024)

We present a theoretical analysis of phase separations between two repulsively interacting components in an ultracold fermionic gas, occurring at the dimensional crossover in a harmonic trap with varying aspect ratios. A tailored kinetic energy functional is derived and combined with a density-potential functional approach to develop a framework that is benchmarked with the orbital-based method. We investigate the changes in the density profile of the phase-separated gas under different interaction strengths and geometries. The analysis reveals the existence of small, partially polarized domains in certain parameter regimes, which is similar to the purely two-dimensional limit. However, the density profile is further enriched by a shell structure found in anisotropic traps. We also track the transitions that can be driven by a change in either interaction strength or trap geometry. The developed framework is noted to have applications for other systems with repulsive interactions that combine continuous and discrete degrees of freedom.

DOI: [10.1103/PhysRevA.110.023325](https://doi.org/10.1103/PhysRevA.110.023325)

I. INTRODUCTION

Reduced-dimensional systems are of great interest in condensed-matter and statistical physics due to the enhanced influence of quantum fluctuations. Such systems are crucial in experimental and technological applications, with examples spanning, e.g., high-temperature superconductors, layered semiconductors, and graphene. Recent advancements in trapping ultracold atomic gases in quasi-two-dimensional geometries [1,2] have enabled the measurement of zero-temperature effects [3–5] and finite-temperature effects [6–10]. This is usually achieved through strongly anisotropic trapping potentials and one-dimensional optical lattices, which allow for the experimental realization of quasi-two-dimensional quantum gases and dimensional crossovers [11–17].

Dimensional crossovers provide access to additional degrees of freedom, leading to the emergence of new quantum states with discrete energies. In quasi-two-dimensional Fermi gases, where the transverse confinement energy is comparable to the Fermi energy, the occupation of new transverse states results in a shell structure [11]. This, in turn, causes steps in the density profile, chemical potential, and specific heat to appear as the system size increases due to the Pauli exclusion principle [11,18–21].

Most of the theoretical and experimental efforts have focused mostly on various many-body effects in two-dimensional Fermi gases, including crossover from Bose-Einstein condensate to Bardeen-Cooper-Schrieffer superfluid [14,22–29], or pairing pseudogap [10,30–32]. As in realistic

experimental scenarios, the anisotropy of confining potentials does not usually allow for a purely two-dimensional regime; therefore, the analysis of dimensional crossovers has been of particular interest [5,11–15,33–37]. Such transitions happen close to the ground state of the considered system and manifest the underlying bonding mechanism in a Fermi gas.

However, when excited, the spin components of a Fermi gas, i.e., given by two chosen hyperfine states, may exhibit repulsive correlations, being brought to the so-called repulsive branch. In the case of a gas trapped in a harmonic potential, that repulsion may lead to a metastable phase separation between the components, an ultracold analog of celebrated Stoner instability in Coulomb-interacting electronic gas [38]. Experimentally elusive in both three and two dimensions due to the eventual decay to the ground state, this itinerant ferromagnetic state has been widely researched both theoretically [39–62] and experimentally [63–73], and also in different mixtures [74–76].

We focus on previously unexplored crossover of the Stoner instability between two and three dimensions, analyzing the purely repulsive system of two fermionic components trapped in an anisotropic trap with varying aspect ratios and interaction strengths. In the three-dimensional limit, the repulsive gas in a radially symmetric trap exhibits both partially and fully polarized phases, whose density profiles remain highly regular, either in a ring structure, with one of the components dominating in the center of the trap, or in two halves separated by a single domain wall [51]. In contrast, in two dimensions, contact-interacting gas can form a plethora of partially polarized states manifesting many small domains, due to a lack of scaling of critical interaction strength with respect to the density of gas in the leading order [59]. In each

*Contact author: piotr.grochowski@upol.cz

of these cases, refined treatment of the kinetic energy, going beyond the usual Thomas-Fermi approach, is necessary, as the competition between the kinetic, interaction, and correlation energies drives the exact shape of the density profile.

To take that into account and to describe systems of sizes reaching usual experimental scenarios of large Fermi clouds, we utilize orbital-free density-potential functional theory (DPFT), which has been proven to accurately determine the complex phases of interacting Fermi gases [77–85]. It achieves this by simplifying the many-body problem to two self-consistent equations: one for the single-particle density and another for an effective potential that accounts for the interactions. DPFT is particularly useful for simulating trapped quantum gases, especially in two-dimensional configurations. Conventional density-functional theory (DFT) techniques are unable to match DPFT’s capabilities in this regard, as they are either limited to small particle numbers [86,87] and periodic confinement [88] or rely on *ad hoc* parametrizations of the kinetic energy [89,90]. Although systematic gradient corrections in two dimensions are available for electronic systems [91], DPFT offers a scalable approach that can be systematically expanded beyond the Thomas-Fermi approximation across one-, two-, and three-dimensional geometries.

In this work we examine phase transitions from para-ferromagnetic states in a binary Fermi gas, involving two- to three-dimensional crossover using density-potential functional theory and Hartree-Fock methods. To this end, we derive a tailored kinetic energy functional for a dimensional crossover of the Fermi gas and combine it with the density-potential functional approach to allow the description of large particle numbers. We use the Hartree-Fock method to benchmark our results in the low-atom-number limit. Our findings indicate highly degenerate ground-state profiles during the transition, featuring various shapes like isotropic and anisotropic separations, ring-shaped polarization, and central splits within a shell structure. These profiles can be manipulated by adjusting particle number, interaction strength, and trapping aspect ratio, offering a versatile exploration of interacting quantum mixtures.

The paper is structured as follows. Section II outlines the derivations of the kinetic and interaction energy functionals for the dimensional crossover, with the analysis of the accuracy given in Appendix A, along with the presentation of the DPFT and Hartree-Fock methods. Section III provides a description of the results we have obtained, including interaction- and aspect-ratio-driven phase transitions, comparison between two methods, and analysis of the large-particle-number limit. We conclude the paper in Sec. IV, providing a summary and outlook for the future.

II. METHODS

A. Density-functional approach for a Fermi gas at a two- to three-dimensional crossover

Let us consider a noninteracting, polarized Fermi gas of N atoms with mass m at zero temperature that is (i) confined in the x - y plane in an area S and (ii) harmonically trapped in the z direction with frequency ω_z . The Hamiltonian of this system

reads

$$\hat{H} = \sum_{i=1}^N \hat{H}_i, \quad (1)$$

where \hat{H}_i is the single-body Hamiltonian that reads

$$\hat{H}_i = \frac{\hat{\mathbf{p}}_i^2}{2m} + \frac{1}{2}m\omega_z^2 \hat{z}_i^2 - \frac{1}{2}\hbar\omega_z, \quad (2)$$

with the two-dimensional momentum operator $\hat{\mathbf{p}}_i$ in the x - y plane, and with the zero-point energy removed. The energy of a single-particle eigenstate reads

$$E_{|\mathbf{k},j\rangle} = \frac{\hbar^2 k^2}{2m} + j\hbar\omega_z, \quad (3)$$

where state $|\mathbf{k}, j\rangle$ is described through the two-dimensional (2D) wave vector \mathbf{k} and the oscillator state number $j \in \{0, 1, \dots\}$. The energy manifolds are degenerate due to both k^2 energy dependence and multiple possible oscillator states. As such, the density of states $\rho(E)$ of the gas can be rewritten as a sum:

$$\rho(E) = \sum_j \rho_j(E) = \sum_j \frac{mS}{2\pi\hbar^2} \theta(E - j\hbar\omega_z), \quad (4)$$

where $\theta(\cdot)$ is a Heaviside step function, summation is performed over available oscillator states, and we have used the expression for two-dimensional density of states $\rho_{2D} = mS/2\pi\hbar^2$. We can then immediately write the total number of atoms as a function of the Fermi energy E_F ,

$$N = \int_0^{E_F} \rho(E) dE = \frac{mS}{2\pi\hbar^2} (l+1) \left(E_F - \frac{1}{2}\hbar\omega_z l \right), \quad (5)$$

where the highest occupied oscillator state number l is introduced through

$$l = \lfloor E_F / \hbar\omega_z \rfloor, \quad (6)$$

where $\lfloor \cdot \rfloor$ is the floor function. Similarly one gets the total energy,

$$\begin{aligned} E_T &= \int_0^{E_F} \rho(E) E dE \\ &= \frac{mS}{4\pi\hbar^2} (l+1) \left[E_F^2 - \frac{1}{3}\hbar^2\omega_z^2 l \left(l + \frac{1}{2} \right) \right]. \end{aligned} \quad (7)$$

Now, combining Eqs. (5) and (7), one can arrive at the Thomas-Fermi energy functional,

$$\epsilon[n_{2D}] = \frac{\pi\hbar^2}{(l+1)m} n_{2D}^2 + \frac{1}{2} l \hbar\omega_z n_{2D} - \frac{l(l+1)(l+2)m\omega_z^2}{48\pi}, \quad (8)$$

where we have introduced the two-dimensional density $n_{2D} = N/S$. As we have gotten rid of E_F from the expression, now l needs to be computed as a solution to

$$\left\lfloor \frac{2\pi\hbar^2}{(l+1)m\hbar\omega_z} n_{2D} + \frac{1}{2} l \right\rfloor = l. \quad (9)$$

Let us now construct the following auxiliary density,

$$n_z(z, n_{2D}) = \sum_j p_j(n_{2D}) n_j(z), \quad (10)$$

which we will use both for comparison of our framework with full three-dimensional density and for derivation of the mean-field energy functional. Here, the densities of oscillator eigenstates,

$$n_j(z) = \frac{1}{2^j j!} \sqrt{\frac{m\omega_z}{\pi\hbar}} e^{-\frac{m\omega_z z^2}{\hbar}} H_j^2\left(\sqrt{\frac{m\omega_z}{\hbar}} z\right), \quad (11)$$

are weighted by the total number of atoms in a given oscillator state,

$$p_j(n_{2D}) = \frac{\int_0^{E_F} \rho_j(E) dE}{\int_0^{E_F} \rho(E) dE} = \frac{1}{l+1} + \frac{m\omega_z}{4\pi\hbar n_{2D}} (l-2j), \quad (12)$$

where $H_j(x)$ is the j th Hermite polynomial. The density n_z is normalized, $\int n_z(z, n_{2D}) dz = 1$.

Let us now consider an additional, slowly varying trapping in the x - y plane, $V(x, y)$, such that the two-dimensional density becomes nonuniform, $n_{2D} = n_{2D}(x, y)$. Then, we approximate the real three-dimensional density $n(x, y, z)$ through

$$n(x, y, z) = n_{2D}(x, y) n_z[z, n_{2D}(x, y)], \quad (13)$$

where $\int n(x, y, z) dx dy dz = N$.

Note that $l = l(x, y)$ now also becomes a position-dependent quantity. We analyze the accuracy of the functional (8) in Appendix A. We show that, at the dimensional crossover in an anisotropic harmonic trap, it outperforms the usual three-dimensional Thomas-Fermi energy functional, both for total energy estimation and predicting the density profile.

Next, we consider a binary mixture of two spin-polarized Fermi gases with densities $n_1(x, y, z)$ and $n_2(x, y, z)$. Let us introduce the total contact interaction energy,

$$E_{\text{int}} = g \int n_1(x, y, z) n_2(x, y, z) dx dy dz, \quad (14)$$

where g is a three-dimensional coupling constant. Then, we can write

$$E_{\text{int}} = \int \epsilon_{\text{int}}[n_1(x, y), n_2(x, y)] dx dy, \quad (15)$$

where $\epsilon_{\text{int}}[n_1(x, y), n_2(x, y)]$ is a two-dimensional interaction energy functional and we dropped the subscript 2D for clarity. Using Eq. (13), the functional can be written as

$$\begin{aligned} \epsilon_{\text{int}}[n_1(x, y), n_2(x, y)] &= g \sqrt{\frac{m\omega_z}{\hbar}} n_1 n_2 \eta_1(l_1, l_2) + g \sqrt{\frac{m\omega_z}{\hbar}} \frac{m\omega_z}{2\pi\hbar} n_1 \eta_2(l_1, l_2) \\ &+ g \sqrt{\frac{m\omega_z}{\hbar}} \frac{m\omega_z}{2\pi\hbar} n_2 \eta_2(l_2, l_1) + g \sqrt{\frac{m\omega_z}{\hbar}} \frac{m^2 \omega_z^2}{4\pi^2 \hbar^2} \eta_3(l_1, l_2), \end{aligned} \quad (16)$$

with

$$\begin{aligned} \eta_1(l_1, l_2) &= \frac{1}{(l_1+1)(l_2+1)} \sqrt{\frac{\hbar}{m\omega_z}} \sum_{j_1, j_2}^{l_1, l_2} \int n_{j_1}(z) n_{j_2}(z) dz, \\ \eta_2(l_a, l_b) &= \frac{1}{l_a+1} \sqrt{\frac{\hbar}{m\omega_z}} \sum_{j_1, j_2}^{l_1, l_2} \left(\frac{l_b}{2} - j_b\right) \int n_{j_a}(z) n_{j_b}(z) dz, \\ \eta_3(l_1, l_2) &= \sqrt{\frac{\hbar}{m\omega_z}} \sum_{j_1, j_2}^{l_1, l_2} \left(\frac{l_1}{2} - j_1\right) \left(\frac{l_2}{2} - j_2\right) \int n_{j_1}(z) n_{j_2}(z) dz. \end{aligned} \quad (17)$$

Here, analogously to Eq. (9), l_1 and l_2 need to be self-consistently solved through

$$\left[\frac{2\pi\hbar^2}{[l_s(x, y) + 1] m \hbar \omega_z} n_s(x, y) + \frac{1}{2} l_s(x, y) \right] = l_s(x, y), \quad (18)$$

with $s \in \{1, 2\}$. With these formulas, we are equipped to construct a density-potential functional theory framework for the dimensional crossover of a Fermi gas that will allow us to include a semilocal kinetic energy description.

B. Density-potential functional theory

The exact DFT energy functional can be rephrased as a bifunctional of the two-dimensional densities \mathbf{n} (here, $\mathbf{n} = \{n_s\} = (n_1, n_2)$ for fermion species $s = 1$ and 2 and from now on we drop the 2D subscript unless stated otherwise) and effective potential energies $\{V_s\}$ that combine the interaction effects with the external potential energies V_s^{ext} [59,82,83,85,92–96]. We find the ground-state densities n_1 and n_2 among the stationary points of this bifunctional by self-consistently solving

$$n_s[V_s - \mu_s](\mathbf{r}) = \frac{\delta E_1[V_s - \mu_s]}{\delta V_s(\mathbf{r})} \quad (19)$$

and

$$V_s[\mathbf{n}](\mathbf{r}) = V_s^{\text{ext}}(\mathbf{r}) + \frac{\delta E_{\text{int}}[\mathbf{n}]}{\delta n_s(\mathbf{r})}. \quad (20)$$

Here, $E_1[V_s - \mu_s]$ is the Legendre transform of the kinetic energy functional $E_{\text{kin}}[n_s]$, μ_s is the chemical potential for species s , and the interaction energy $E_{\text{int}}[\mathbf{n}]$ generally couples all densities. For the general formalism and many applications of this DPFT we refer to Refs. [59,82,83,85,92–96] and references therein. In particular, we deploy the exact same machinery for two-component interacting fermion gases as in Ref. [59], with the twist of transferring the kinetic energy contribution that stems from the transversal direction to the interaction energy. This augmentation of the DPFT framework allows us to predict the properties of 3D systems at the cost of 2D calculations.

Specifically, by adding and subtracting the TF kinetic energy density $\epsilon_{\text{kin}}^{\text{TF}, 2D} = \pi \hbar^2 n^2 / m$ for spin-polarized fermions in

2D, we write the full energy density (8) as

$$\epsilon[n] = \epsilon_{\text{kin}}^{\text{TF,2D}} + \epsilon_{\text{int}}^{\text{2D3D}}. \quad (21)$$

Here, the effective interaction energy density

$$\epsilon_{\text{int}}^{\text{2D3D}} = -\frac{\pi\hbar^2}{m} \frac{l}{l+1} n^2 + \frac{1}{2} \hbar l n \omega_z - \frac{m\omega_z^2}{48\pi} l(l+1)(l+2) \quad (22)$$

compensates for the introduction of the 2D TF kinetic energy in Eq. (21). Since $l(n)$ is piecewise constant, the functional derivative of the energy $E_{\text{int}}^{\text{2D3D}}[n] = \int d\mathbf{r} \epsilon_{\text{int}}^{\text{2D3D}}$ is

$$\frac{\delta E_{\text{int}}^{\text{2D3D}}[n]}{\delta n(\mathbf{r})} = \frac{-2\pi\hbar^2 n(\mathbf{r})l}{m(l+1)} + \frac{\hbar\omega_z l}{2}, \quad (23)$$

which we incorporate into the effective interaction potential in Eq. (20), such that we can execute the self-consistent program of Eqs. (19) and (20) in a pure 2D setting.

Finally, we may replace the quasiclassical TF kinetic energy $E_{\text{kin}}^{\text{TF,2D}}$ by semiclassical approximations of the (Legendre-transformed) kinetic energy functional, viz., approximations of $E_1[V - \mu]$; all details of the numerical procedures are discussed in Ref. [59]. Accordingly, we deploy the nonlocal quantum-corrected successor

$$n_{3'}(\mathbf{r}) = \int (d\mathbf{r}') \left(\frac{k_{3'}}{2\pi r'} \right)^D J_D(2r' k_{3'}) \quad (24)$$

of the local TF density for D dimensions (see Refs. [59,84]), with the Bessel function $J_D(\cdot)$ of order D and the effective Fermi wave number

$$k_{3'} = \frac{1}{\hbar} \{2m[\mu - V(\mathbf{r} + \mathbf{r}')]\}_+^{1/2}, \quad (25)$$

where $[z]_+ = z \Theta(z)$, and $\Theta(\cdot)$ is the Heaviside step function.

The approximate DPFT framework introduced here can be applied in situations where the qualitatively different treatment of E_{int} [with the quasiclassical TF approximation, Eq. (22)] and E_{kin} [with the semiclassical $n_{3'}$ density formula, Eq. (24)] is acceptable. We determine to which extent this holds true by benchmarking $n_{3'}$ -based DPFT densities against Hartree-Fock (HF) results.

C. Orbital approach

To perform this benchmark, we use time-dependent HF equations,

$$i\hbar \frac{\partial}{\partial t} \varphi_i^{(s)}(\mathbf{r}, t) = \left[-\frac{\hbar^2}{2m} \nabla^2 + V_s^{\text{ext}}(\mathbf{r}, t) \frac{\delta E_{\text{int}}[\mathbf{n}]}{\delta n_s(\mathbf{r}, t)} \right] \varphi_i^{(s)}(\mathbf{r}, t), \quad (26)$$

for the two-component spin mixture ($s \in \{1, 2\}$). The derivation of these equations is shown in Appendix B. Here, $\varphi_i^{(1)}(\mathbf{r}, t)$ and $\varphi_i^{(2)}(\mathbf{r}, t)$, with $i = 1, \dots, N/2$, are spatial orbitals of the first and the second spin component, respectively. The interaction terms $\frac{\delta E_{\text{int}}[\mathbf{n}]}{\delta n_{1/2}(\mathbf{r}, t)}$ are defined below through Eq. (14). The one-particle densities

$$n_s(\mathbf{r}, t) = \sum_{i=1}^{N/2} |\varphi_i^{(s)}(\mathbf{r}, t)|^2 \quad (27)$$

associated with the spin components s sum to the total one-particle density $n(\mathbf{r}, t) = n_1(\mathbf{r}, t) + n_2(\mathbf{r}, t)$.

We are looking for the ground-state densities. We are solving the set of Eqs. (26) by the imaginary time propagation technique [97] where real time is replaced by imaginary time $t \rightarrow -i\tau$. After that, the evolution operator is no longer a unitary operator. Both the norm and the orthogonality are lost during the imaginary time propagation. To keep the orthogonality and the norm of the spatial orbitals we use the Gram-Schmidt orthonormalization technique. This way, by propagating N spatial orbitals we obtain the ground state of N particles.

III. RESULTS

Our focus lies predominantly on analyzing phase transitions in a binary Fermi gas, dependent on three key physical parameters: the number of particles N , the aspect ratio λ , and the strength of three-dimensional interactions g . Specifically, we consider a balanced two-component Fermi gas at zero temperature; each component consisting of $N_1 = N_2 = N/2$ atoms and trapped in the anisotropic harmonic potential with aspect ratio $\lambda = \omega_z/\omega$,

$$V(x, y, z) = \frac{1}{2} m \omega^2 (x^2 + y^2 + \lambda^2 z^2). \quad (28)$$

Both species interact via contact repulsion given by three-dimensional pairwise delta interaction characterized by the coupling constant $g = 4\pi a \hbar^2/m$, where a is the scattering length. Here, we focus only on a mean-field contribution (14) coming from this interaction, hence neglecting quantum contributions that stem from the exact, many-body ground state. In the case of the repulsive binary Fermi mixture, such an omission shifts the critical values of interaction strengths at which phase transitions happen, in both the two-dimensional geometry [59] and the three-dimensional geometry [76]; however, qualitative features are left unchanged for nonuniform mixtures. The refinement of the energy spectrum of repulsive Fermi gas beyond the mean field has been performed via many different approaches, including perturbation theory [41,98,99], quantum Monte Carlo simulations [43,45,46,100–104], lowest-order constraint variational calculation [105], nonperturbative ladder approximation [106], large- N expansion, dimensional ϵ -expansion [107], and the polaronic approach [108,109]. However, most efforts have focused on either the purely two-dimensional limit or the purely three-dimensional limit, while dimensional crossover has been analyzed only for attractive mixtures [5,11–15,33–37]. As such, we focus on the mean-field description of interaction and leave further refinement as an outlook.

The transitions we consider manifest as distinct phase separations in the ground-state densities of the gas components. Past research has highlighted that in radially symmetric harmonic trapping, transitions occur from uniform density profiles of the two fermion species to both isotropic and anisotropic separations. Furthermore, within a purely two-dimensional configuration with bare contact interaction, an analogous transition arises [59]. This transition shifts from a paramagnetic state at low repulsive interactions to ferromagnetic density profiles at higher interaction strengths. However,

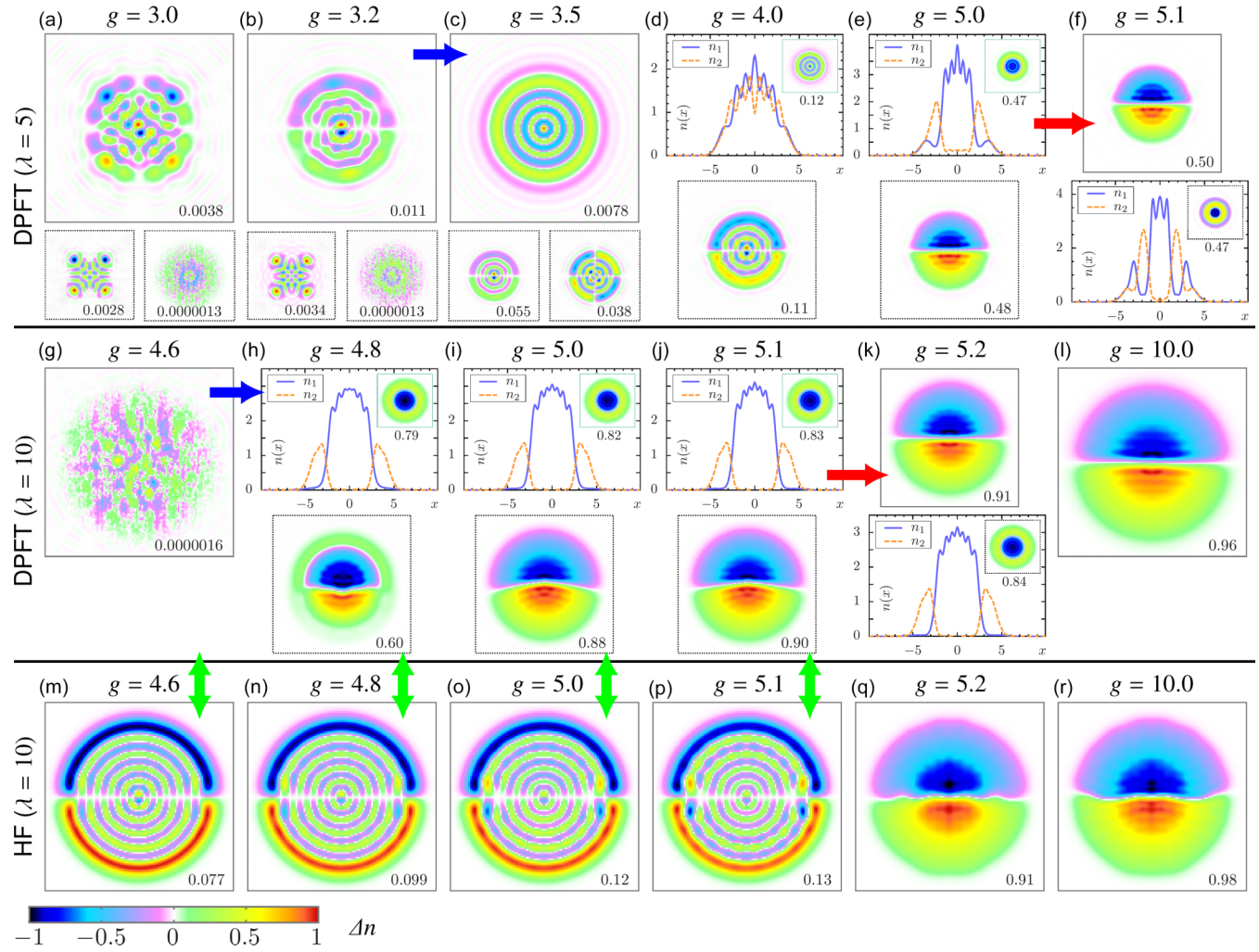


FIG. 1. The density profiles for a two-component repulsive Fermi gas across interaction-driven phase transitions. The top (bottom) plots in each panel present the ground-state (metastable, closely matched in energy) profiles. The density profiles are plotted either as scaled density differences $\Delta n = (n_1 - n_2) / \max_r |n_1(\mathbf{r}) - n_2(\mathbf{r})|$, which are presented as contour plots in a square box with edge lengths of 6 (we use harmonic oscillator units $\hbar = m = \omega = 1$; the color legend applies to all the contour plots), or as density cross sections at $y = 0$. (a)–(f) Ground-state density profiles for a fixed aspect ratio of the harmonic trap ($\lambda = 5$) and a constant total number of particles ($N_1 = N_2 = 55$). These profiles vary with the three-dimensional repulsive coupling constant between the two species, denoted as g , and their absolute density differences can be characterized through a global polarization \mathcal{P} [defined through Eq. (29) and displayed in the bottom right corner of each of the plots]. Notably, two distinct phase transitions are observable: one from a paramagnetic to an isotropic, partially polarized phase (marked by blue arrows), followed by a transition to a two-hemisphere state (red arrows). The findings are obtained using a density-potential functional approach. (g)–(l) Similarly presented are ground-state density profiles for a higher aspect ratio of the trap ($\lambda = 10$). (m)–(r) The results in this row are analogous to those in the second row; however, they are computed using the Hartree-Fock approach. Although the weak- and large-interaction limits yield comparable outcomes, disparities become evident within the phase transition regime (green arrows). See Table I for details of each panel, including interaction strength, scaling factor, energy, polarization, and transverse excitations.

intricate particle-number-dependent phases emerge between these limits. Moreover, a range of metastable configurations with energy levels comparable to ground-state density profiles have been identified within the transitional regime. These configurations are likely to be observed in experimental settings. Hence, our analysis seeks to uncover the crossover between these two scenarios, achievable by transitioning dimensionally through adjustments in the trap's aspect ratio. For the analysis of spatial separation at the crossover, we utilize a total polarization \mathcal{P} of the trapped mixture:

$$\mathcal{P} = \frac{\int d\mathbf{r} |n_1(\mathbf{r}) - n_2(\mathbf{r})|}{N}. \quad (29)$$

A. Interaction-driven phase transitions

We begin by examining a specific scenario where we vary interaction strengths while keeping the aspect ratio $\lambda = 5$ and the particle count $N_1 = N_2 = 55$ constant. We present it in Figs. 1(a)–1(f). At low interaction strengths, a paramagnetic phase is observed, where nearly identical density profiles with accordingly small energy differences make it difficult to distinguish the ground state from metastable states. Although overall polarization remains low, as we increase the interaction strength to around $g = 3.5$, slight polarization modulations emerge near the center due to a relative decrease in interaction energy at the expense of kinetic energy. At

$g = 3.5$ this trade-off between the energy components begins to favor ground-state profiles with isotropic separations. This transition is characterized by visible domains without breaking radial symmetry. We identify states in close energy proximity that break radial symmetry and possess nonzero polarization. These states bear a resemblance to findings in purely 2D scenarios. Further along, as the interaction strength reaches $g = 5$, the gas segregates into two hemispheres, mirroring the analogous behavior observed in both 2D and 3D.

Subsequently, we compare these results with those from an altered aspect ratio, $\lambda = 10$ [refer to Figs. 1(g)–1(l)]. We observe analogous behavior; however, the initial transition from no separation to isotropic separation is more pronounced, lacking an easily distinguishable transitional regime characterized by minor polarization modulations. This transition occurs at $g = 4.65$ and is followed by a mirror-symmetric separation at $g = 5.15$ that grows into an almost complete split separation at $g = 10$. Again, we find metastable states across the transitions, which show competition between different types of splittings. However, for this particular aspect ratio and atom number, the competition is mainly between isotropic and anisotropic separation states.

These findings are consistent with both two- and three-dimensional cases; however, they indicate that the fine structure of coexisting metastable states strongly depends on the perpendicular excitation structure. Symmetry-breaking partially polarized profiles are unveiled for lower aspect ratios when the perpendicular degree of freedom is more intensely excited, in contrast to the higher aspect ratio case where such structures are not easily discernible (cf. Table I). This showcases nontrivial behavior, similar to the scenario in the limit of pure two-dimensional geometry where these metastable states are present.

B. Benchmarking DPFT against Hartree-Fock

We now move on to validate the previously described low-atom-number outcomes using the orbital approach. We compare density profiles throughout the interaction-induced phase transition for $\lambda = 10$ and $N_1 = N_2 = 55$, as displayed in Figs. 1(m)–1(r). While we observe that within the weak-interaction limit, the paramagnetic, identical density profiles of both clouds are consistent across both methods, a slight discrepancy emerges at the onset of the phase transition. The isotropic transition is not evident, but instead, the ground state just above the transition assumes a partially polarized, symmetry-breaking configuration. It is worth noting that the density structure of this state bears a resemblance to certain profiles of metastable states identified using the DPFT method. This observation suggests that the ground state at the transition is nearly degenerate, with various density profiles being realized by states with minute energy differences. We hypothesize that the divergence between the methods regarding the true ground state arises from the proximity of these states. Importantly, in Hartree-Fock calculations, the subsequent phase transition to a two-hemisphere state occurs at a similar value of the interaction strength as observed in the DPFT method. In the scenario of a large-interaction limit, density profiles between the two methods align remarkably well.

To conduct a more comprehensive analysis of this comparison, we present in Fig. 2 the comparison between the two methods across both interaction and aspect ratio variations. We employ the total energy, the total polarization, and the ratio between interaction and kinetic energies as metrics for assessment. First, we find that energies match very well across both transitions, suggesting consistency between both methods. As for the total polarization and the energy ratio, the behavior across the transition is qualitatively captured with a good quantitative match in the strong-coupling regime. This slight quantitative mismatch suggests that the total polarization is a sensitive probe for specifying which state is realized experimentally. Importantly, comparing the cuts through the density profiles, we find that the slopes of the density profiles match in both methods, implying a mutually consistent description of the interplay of kinetic and interaction energies in both methods. Such a behavior is of particular interest as the domain-wall density profile determines, e.g., dimer formation rates in ultracold gases.

C. Large-atom-number limit

We now proceed to analyze large-atom-number setups that go beyond the manageability of the Hartree-Fock approach due to numerical cost. In Fig. 3 we present two cases, $N_1 = N_2 = 500$ and $N_1 = N_2 = 5000$, both computed with the DPFT approach. In these cases, the shell structure of the density profiles, usual in low-dimensional experimental setups, i.e., sharp transitions in the densities due to discretized energy spectrum in the transversal direction, becomes apparent. First, we observe that the existence of these sharp density changes makes the competition between kinetic and interaction energy even more intricate. As we go through the interaction-induced transition for $N_1 = N_2 = 500$, we find that partial polarization may be favored at these density changes, revealing a ring-shaped polarization pattern that might or might not preserve radial symmetry. As the interaction strength increases above $g \approx 1.4$, the preferred density profile involves the anisotropic split at the center of the trap and a shell structure at the perimeter. With the further growing interaction, this central split occupies more volume, becoming two fully separated hemispheres in the strong-interaction regime. Notably, in this case, no ground-state isotropic separation is observed. The $N_1 = N_2 = 5000$ case exhibits similar behavior. Across the phase transition toward a ferromagnetic state, one observes the coexistence of both isotropic and anisotropic ring-shaped polarization structures and the central anisotropic split, shown in the lower-atom-number case.

D. Geometry-driven transitions

Up to now, we have analyzed a phase transition driven by the varying interaction. Here, we would like to focus on the case in which the ground-state density profile is altered through the change of geometry via the aspect ratio of the harmonic trap. In Fig. 4 we plot the transition for $g = 5.5$ and $N_1 = N_2 = 55$, while the aspect ratio is changed from $\lambda = 3$ to $\lambda = 15$ [compare Fig. 2(h), where the total polarization is plotted for this transition]. Such a sweep realizes a transition from a partially polarized anisotropic split to the fully

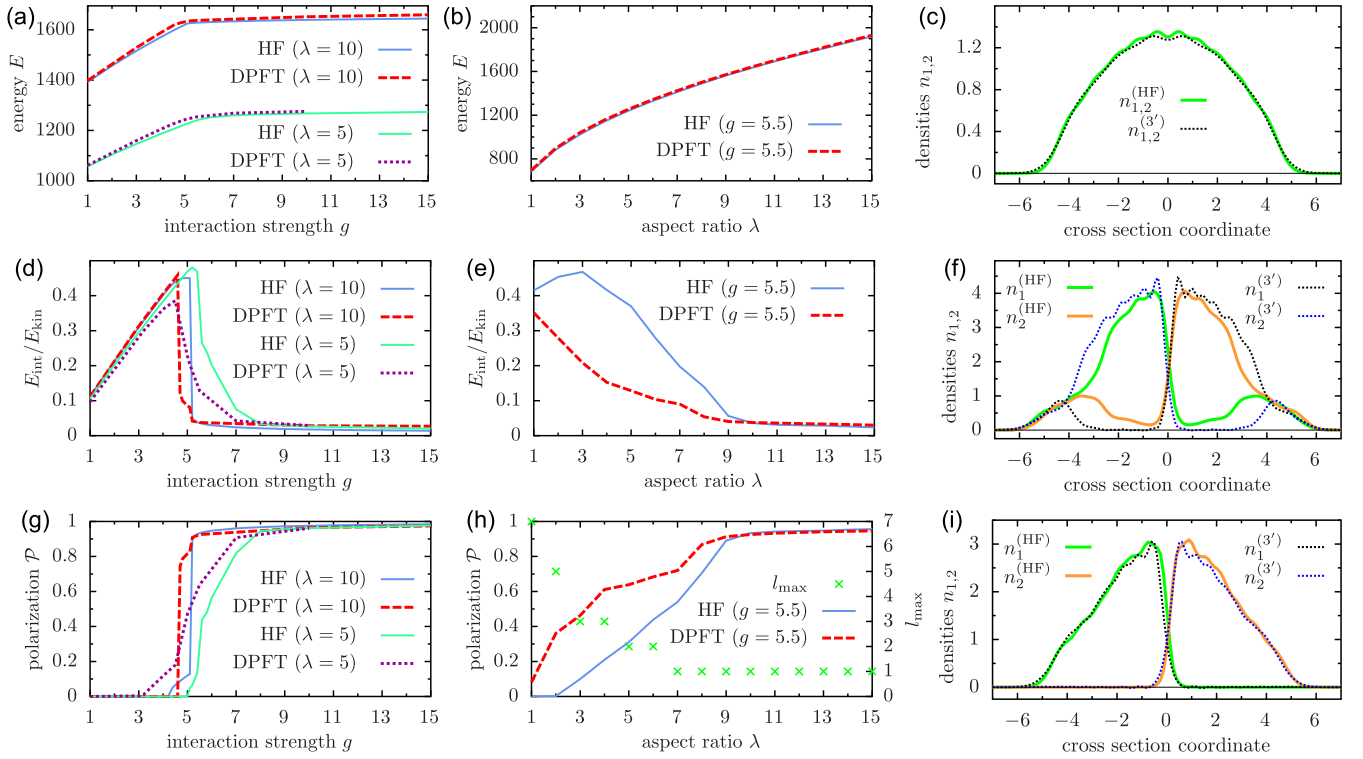


FIG. 2. (a), (b) Total energy of a two-component Fermi gas throughout interaction and aspect ratio sweeps for two methods—density-potential functional theory and Hartree-Fock. Both methods show similar predictions. (d), (e), (g), (h) The same but for the ratio between interaction and kinetic energies (d), (e) and for the total polarization (g), (h). In these cases, the two methods match for strong interactions and high aspect ratios, but otherwise they yield density profiles with quite different polarizations and energy ratios—a sign of near-degenerate states across the transitions with respect to g and λ . (c), (f), (i) Comparison of density cross sections for both methods. The slopes of the densities match very well for weakly and strongly interacting clouds, displaying some mismatch in the transitional regime. We use harmonic oscillator units $\hbar = m = \omega = 1$.

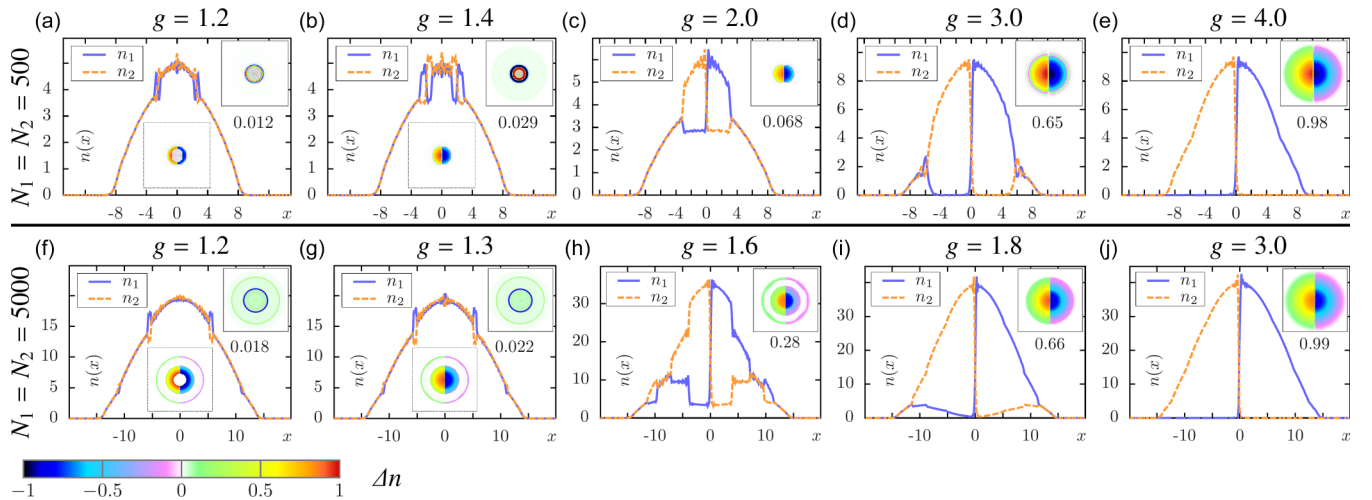


FIG. 3. (a)–(e) Ground-state density profiles for a two-component repulsive Fermi gas, with a fixed aspect ratio of the harmonic trap ($\lambda = 25$) and a constant total number of particles ($N_1 = N_2 = 500$). These profiles vary with the three-dimensional repulsive coupling constant between the two species, denoted as g . A richer density profile structure across the para- to ferromagnetic phase transition is visible, as compared to the lower atom number case, exhibiting ring-shaped polarization and central-split patterns. (f)–(j) The same but for $\lambda = 30$ and $N_1 = N_2 = 5000$. The density profile gets even more intricate, showing the coexistence of ring-shaped polarization and central-split patterns for some values of interaction strength. The main plot and the top right inset in each panel present the ground-state profiles. In panels (a), (b), (f), and (g), we also show metastable profiles. The scaled density differences $\Delta n = (n_1 - n_2)/\max_r |n_1(\mathbf{r}) - n_2(\mathbf{r})|$ are presented as contour plots in a square box with edge lengths of 10 (15) for $N_{1/2} = 500$ ($N_{1/2} = 5000$); we use harmonic oscillator units $\hbar = m = \omega = 1$ and the color legend applies to all the contour plots. See Table II for details.

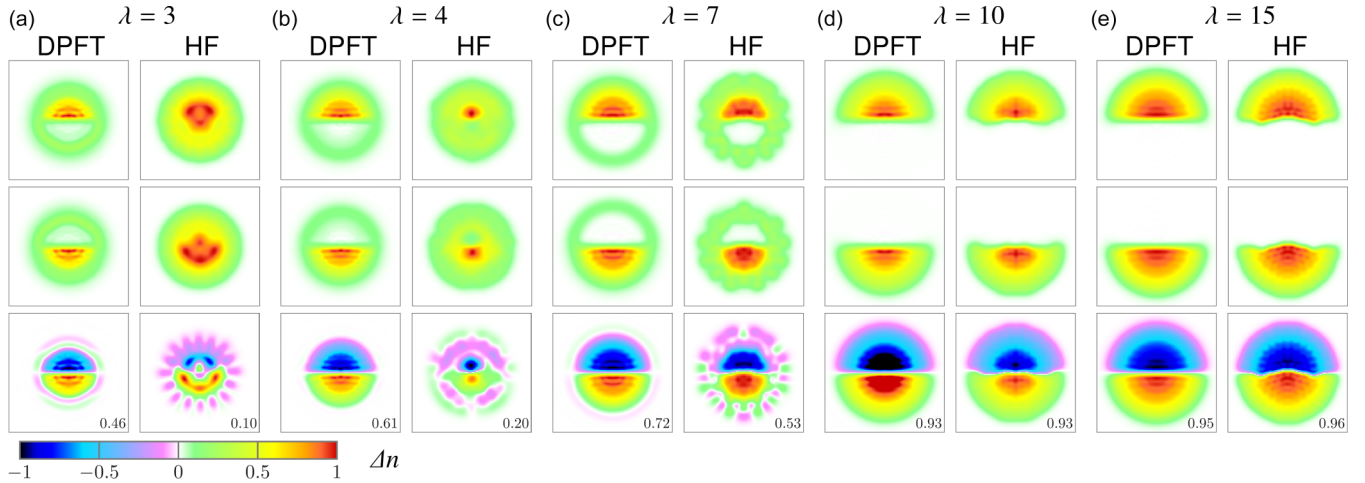


FIG. 4. Ground-state density profiles for a two-component repulsive Fermi gas, with a fixed coupling constant between two fermionic components ($g = 5.5$) and a constant total number of particles ($N_1 = N_2 = 55$). These profiles vary with the aspect ratio of the harmonic trap λ , exhibiting a transition from a partially polarized state to a fully polarized state. The top (bottom) plots in each panel present the ground-state (metastable) profiles. The scaled density differences $\Delta n = (n_1 - n_2) / \max_r |n_1(\mathbf{r}) - n_2(\mathbf{r})|$ are presented as contour plots in a square box with edge lengths of 6; we use harmonic oscillator units $\hbar = m = \omega = 1$ and the color legend applies to all the contour plots. See Table III for details.

separated hemispheres. In the limiting cases, the phase separation occurs at $g \approx 7$ for $\lambda = 1$ [51] and at $g \approx 15.7/\sqrt{\lambda}$ for the two-dimensional limit $\lambda \rightarrow \infty$ [59] (which equals $g = 5.0$ and $g = 4.1$ for $\lambda = 10$ and $\lambda = 15$, respectively). It shows how the geometry can be used to drive the phase transition, similarly to experiment with, e.g., confinement-induced resonances [110].

IV. CONCLUSIONS AND OUTLOOK

Summarizing, we have analyzed para- to ferromagnetic phase transition in a binary zero-temperature repulsive Fermi gas at a two- to three-dimensional crossover utilizing two distinctive methods—the density-potential functional theory and Hartree-Fock methods. We have found out that in a quasi-two-dimensional regime, the ground-state profile across the phase transition is nearly degenerate and exhibits a variety of shapes, including isotropic and anisotropic separations, ring-shaped polarization patterns, and central-split patterns in the usual shell structure. These density profiles can be tuned via means of varying the particle number, the interaction strength, and the aspect ratio of the external trapping, providing a versatile playground for the physics of interacting quantum mixtures.

As argued above, we have omitted the quantum corrections to the mean-field interaction that would shift the values of the interaction strength at which the transitions happen. The inclusion of these corrections will be a subject of future work. Another limitation of the considered model comes from the neglect of thermal excitations—in the context of itinerant ferromagnetism and phase separations in ultracold gases, finite-temperature effects have been considered for Fermi-Fermi [49,55,60,111] and Bose-Fermi [76] mixtures in two and three dimensions, repulsive polarons [49,112], many-component mixtures [113], and dipolar gases [114]. Nonzero temperature results in the shift of the critical value of the interaction strength towards higher values of the interaction [49,55,60,69], it can change the order of transition [113],

and, if sufficiently large, thermal fluctuations make the phase separation disappear [49]. In the case we consider, exhibiting a plethora of fine-polarization patterns, finite temperature would most likely additionally smear out small density fluctuations, similar to what we observed in two dimensions [59]. However, such an analysis is outside of the scope of this work and is left out as an outlook for the future.

The experimental realizations of a two-component repulsive Fermi mixture in two and three dimensions, both single-element and two-element, have been presented with many different species, including lithium [11,65,69,70,73,115], potassium [116–118], chromium [119], ytterbium [120], and dysprosium [121]. These realizations provide a natural experimental testbed for fermionic phase separation due to repulsion, also beyond the considerations of this work—involving different mass ratios and mixtures with different species—so that competing effects such as molecule formation could be suppressed and ferromagnetic correlations revealed. Another avenue for fermionic phase separation involves repulsive Bose-Fermi mixtures that have recently gained momentum, both theoretically [75,76,122,123] and experimentally [74,124].

As a concluding remark, it is worth noting that the multiparticle Hamiltonian governing the system in this paper exhibits axial symmetry. This implies that, unless degenerate, the ground state must also possess axial symmetry. However, the observed symmetry-breaking single-particle patterns, detailed in this study, are entirely physical as they accurately describe individual experimental shots. This somewhat paradoxical aspect of the density functional method was recently highlighted in Ref. [125].

ACKNOWLEDGMENTS

The Center for Theoretical Physics of the Polish Academy of Sciences is a member of the National Laboratory of Atomic, Molecular and Optical Physics (KL FAMO). This

work has been supported by the National Research Foundation, Singapore, and A*STAR under its CQT Bridging Grant and its Quantum Engineering Programme. Part of the results were obtained using computers of the Computer Center of the University of Białystok.

APPENDIX A: TESTING THE ENERGY FUNCTIONAL IN THE NONINTERACTING CASE

Let us consider a noninteracting spin-polarized Fermi gas trapped in an anisotropic harmonic trap with an aspect ratio λ ,

$$V(x, y, z) = \frac{1}{2}m\omega^2(x^2 + y^2 + \lambda^2 z^2). \quad (\text{A1})$$

The ground state of the gas is given by a Slater determinant of N lowest-energy harmonic single-particle eigensolutions,

$$\begin{aligned} \psi_{ijk}(x, y, z) &= \psi_i(x)\psi_j(y)\lambda^{1/4}\psi_k(\lambda^{1/2}z), \\ \psi_i(x) &= \frac{1}{\sqrt{2^i i!}} \left(\frac{m\omega}{\pi\hbar} \right)^{1/4} e^{-\frac{m\omega x^2}{2\hbar}} H_i \left(\sqrt{\frac{m\omega}{\hbar}} x \right), \end{aligned} \quad (\text{A2})$$

with a single-particle energy $E_{ijk} = \hbar\omega(i + j + \lambda k + 1)$, where again we subtracted the zero-point energy of the z mode. The total energy of the gas then reads

$$E_{\text{ex}} = \sum_{n=1}^N E_n, \quad (\text{A3})$$

where $E_n = E_{ijk}$ and the associated single-particle wave function $\psi_n = \psi_{ijk}$ are ordered such that $E_{n+1} \geq E_n$. The single-particle density $n_{\text{ex}}(x, y, z)$ then can be expressed as

$$n_{\text{ex}}(x, y, z) = \sum_{n=1}^N |\psi_n(x, y, z)|^2, \quad (\text{A4})$$

and we can additionally define a column density,

$$n_{2\text{D}}^{\text{ex}}(x, y) = \int dz n_{\text{ex}}(x, y, z). \quad (\text{A5})$$

To get a closed expression for each of these quantities in the large- N limit, one can resolve to utilize a Thomas-Fermi approximation along with the local density approximation. Here, we compare the functional introduced in Sec. II A and the usual approach involving a three-dimensional Thomas-Fermi functional,

$$E_{\text{TF}}[n, \mu] = E_{\text{kin}} + E_{\text{pot}} + \mu \left(N - \int dx dy dz n(x, y, z) \right), \quad (\text{A6})$$

with

$$\begin{aligned} E_{\text{kin}}[n, \mu] &= A \int dx dy dz n^{5/3}(x, y, z), \\ E_{\text{pot}}[n, \mu] &= \int dx dy dz n(x, y, z) V(x, y, z), \end{aligned} \quad (\text{A7})$$

where $A = 6^{5/3} \hbar^2 \pi^{4/3} / 20m$ and μ is a chemical potential. The minimization of Eq. (A6) yields the following Thomas-Fermi equations:

$$\frac{3}{5} A n^{2/3}(x, y, z) = \mu - V(x, y, z). \quad (\text{A8})$$

They can be readily solved to obtain

$$\begin{aligned} n_{\text{TF}}(x, y, z) &= \left(\frac{3}{5} A^{-1} \right)^{3/2} [\mu_{\text{TF}} - V(x, y, z)]^{3/2}, \\ \mu_{\text{TF}} &= 6^{1/3} \hbar\omega N^{1/3} \lambda^{1/3}, \\ n_{2\text{D}}^{\text{TF}}(r) &= \frac{m}{4\pi\omega\lambda\hbar^3} \left(\mu_{\text{TF}} - \frac{1}{2} m\omega^2 r^2 \right)^2, \\ E_{\text{TF}} &= 3^{4/3} 2^{-5/3} \hbar\omega N^{4/3} \lambda^{1/3} - E_0, \end{aligned} \quad (\text{A9})$$

where $r = \sqrt{x^2 + y^2}$, E^{TF} is a total energy with subtracted zero-point contribution of the z mode, and $E_0 = \frac{1}{2} \hbar\omega N \lambda$. Similar minimization for Eq. (8) gives

$$\begin{aligned} n_{2\text{D}}(r) &= \frac{m}{2\pi\hbar^2} \begin{cases} \mu_{2\text{D}} - \frac{1}{2} m\omega^2 r^2, & r_1 < r < r_0, \\ \dots \\ (j+1)(\mu_{2\text{D}} - \frac{1}{2} m\omega^2 r^2 - \frac{1}{2} j\lambda\hbar\omega), & r_{j+1} < r < r_j, \\ \dots \\ (l_m+1)(\mu_{2\text{D}} - \frac{1}{2} m\omega^2 r^2 - \frac{1}{2} l_m\lambda\hbar\omega), & 0 < r < r_{l_m}, \end{cases} \\ \mu_{2\text{D}} &= \hbar\omega \frac{3l_m(l_m+1)\lambda + \sqrt{72(l_m+1)N - 3l_m(l_m+1)^2(l_m+2)\lambda^2}}{6(l_m+1)}, \\ E_{2\text{D}} &= \hbar\omega \frac{l_m+1}{24} \left[l_m^2(l_m+1)\lambda^3 - \frac{1}{9} \left(3l_m\lambda + \sqrt{\frac{72N}{l_m+1} - 3l_m(l_m+2)\lambda^2} \right)^2 \left(\frac{1}{2} l_m\lambda - \frac{1}{3} \sqrt{\frac{72N}{l_m+1} - 3l_m(l_m+2)\lambda^2} \right) \right], \end{aligned} \quad (\text{A10})$$

where l_m is given implicitly through

$$l_m = \left\lfloor \frac{1}{2} l_m + \frac{1}{6\lambda} \sqrt{\frac{72N}{l_m+1} - 3l_m(l_m+2)\lambda^2} \right\rfloor. \quad (\text{A11})$$

One can find an asymptotic behavior,

$$l_m \xrightarrow{N/\lambda^2 \rightarrow \infty} 6^{1/3} N^{1/3} \lambda^{-2/3}, \quad (\text{A12})$$

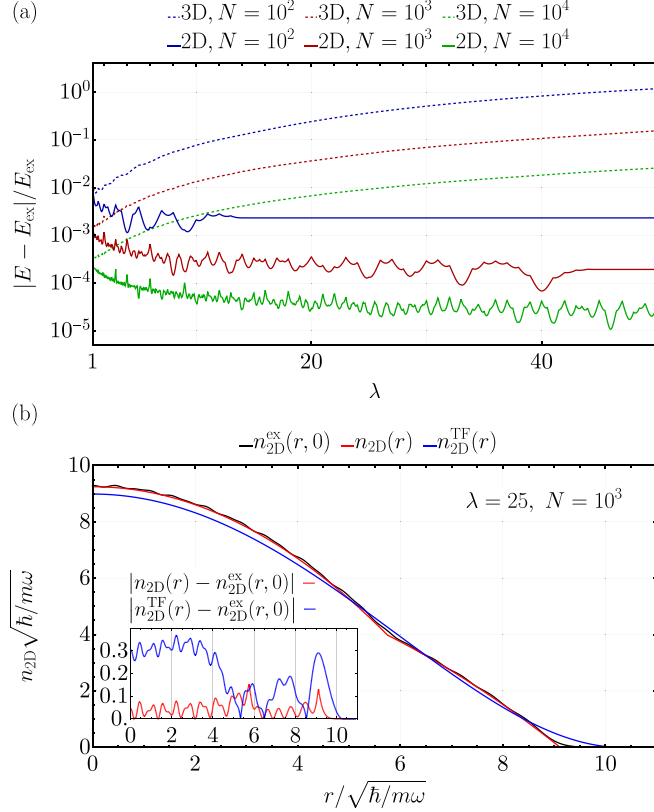


FIG. 5. (a) Comparison of energies obtained through minimization of either functional (8) (label 2D, solid lines) or functional (A6) (label 3D, dashed lines) with respect to the exact energy (A3) for different trap anisotropies λ and atom numbers N . The former function provides more accurate results with the highest difference at large anisotropies. (b) Comparison of the density profiles obtained through two methods [given through Eqs. (A10) and (A9)] and the exact profile (A5) for $\lambda = 25$ and $N = 1000$. The density profile exhibits a sharp transition around $r/\sqrt{\hbar/m\omega} = 5.5$ that is reproduced only with the former method. Inset: Absolute density differences between the two methods and the exact density value.

from which other asymptotics follow:

$$\begin{aligned} \mu_{2D} &\xrightarrow{N/\lambda^2 \rightarrow \infty} \mu_{\text{TF}}, \\ E_{2D} &\xrightarrow{N/\lambda^2 \rightarrow \infty} E_{\text{TF}} + E_0, \\ n_{2D}(r_j) &\xrightarrow{N/\lambda^2 \rightarrow \infty} n_{2D}^{\text{TF}}(r_j), \end{aligned} \quad (\text{A13})$$

showing that in the limit of a large number of atoms and low trap anisotropy, the two approaches tend to the same solution. If N is taken to be finite, then the two methods differ. We present the comparison in Fig. 5, showing that the usual three-dimensional Thomas-Fermi approach is less accurate for the energy estimation and does not reproduce the sharp features of the density profile appearing due to the change of transverse states.

APPENDIX B: DERIVATION OF TIME-DEPENDENT HARTREE-FOCK EQUATIONS

In HF approximation one assumes that N fermions are described by the wave function in the following form:

$$\Psi = \frac{1}{\sqrt{N!}} \begin{vmatrix} \psi_1(1) & \psi_1(2) & \dots & \psi_1(N) \\ \psi_2(1) & \psi_2(2) & \dots & \psi_2(N) \\ \vdots & \vdots & \ddots & \vdots \\ \psi_N(1) & \psi_N(2) & \dots & \psi_N(N) \end{vmatrix}, \quad (\text{B1})$$

where $\psi_i(j)$ are spin orbitals. In general, the spin orbital can be written as

$$\psi_i(j) = \begin{bmatrix} \varphi_i(1, \mathbf{r}_j, t) \\ \varphi_i(2, \mathbf{r}_j, t) \\ \vdots \\ \varphi_i(s, \mathbf{r}_j, t) \end{bmatrix}, \quad (\text{B2})$$

where $\varphi_i(s_j, \mathbf{r}_j, t)$ are spatial orbitals. The spin orbitals fulfill the orthonormality condition

$$\langle \psi_i | \psi_k \rangle = \sum_{s_j=1}^{s_{\text{max}}} \int \varphi_i^*(s_j, \mathbf{r}_j, t) \varphi_k(s_j, \mathbf{r}_j, t) d\mathbf{r}_j = \delta_{ik}, \quad (\text{B3})$$

TABLE I. Details for the density plots in Figs. 1(a)–1(r).

Panel	λ	g	$\max_r n_1(\mathbf{r}) - n_2(\mathbf{r}) $	E	\mathcal{P}	(l_1, l_2)
a	5	3	0.0460	1159.34	0.0038	(1,1)
			0.0389	1159.35	0.0028	(1,1)
			1.7×10^{-5}	1159.41	1.3×10^{-6}	(1,1)
b	5	3.2	0.194	1168.62	0.0114	(1,1)
			0.0455	1168.62	0.0034	(1,1)
			1.6×10^{-5}	1168.73	1.3×10^{-6}	(1,1)
c	5	3.5	0.0652	1182.17	0.0078	(1,1)
			1.1500	1182.20	0.0552	(1,1)
			0.3417	1182.30	0.0380	(1,1)
d	5	4	1.3240	1204.50	0.1174	(1,1)
			1.0176	1204.60	0.1086	(1,1)
e	5	5	3.9239	1242.91	0.4702	(1,2)
			3.4668	1242.91	0.4773	(2,2)
f	5	5.1	3.6025	1245.63	0.5049	(2,2)
			3.7670	1247.33	0.4700	(2,2)
g	10	4.6	1.8×10^{-5}	1621.74	1.6×10^{-6}	(0,0)
h	10	4.8	2.9592	1627.06	0.7875	(0,1)
			3.0182	1629.09	0.6039	(1,1)
i	10	5	3.0595	1631.64	0.8156	(0,1)
			3.0144	1633.82	0.8762	(1,1)
j	10	5.1	3.1148	1633.91	0.8254	(0,1)
			3.0375	1634.71	0.8986	(1,1)
k	10	5.2	3.0632	1635.45	0.9083	(1,1)
			3.1545	1636.47	0.8357	(0,1)
l	10	10	3.2809	1651.59	0.9644	(1,1)
m	10	4.6	0.2606	1601.00	0.0774	—
n	10	4.8	0.3432	1610.79	0.0995	—
o	10	5	0.4113	1620.26	0.1193	—
p	10	5.1	0.4524	1624.87	0.1281	—
q	10	5.2	3.0423	1626.40	0.9086	—
r	10	10	3.1390	1639.25	0.9755	—

TABLE II. Details for the density plots in Figs. 3(a)–3(j).

Panel	$N_1 = N_2$	λ	g	$\max_r n_1(\mathbf{r}) - n_2(\mathbf{r}) $	E	\mathcal{P}	(l_1, l_2)
a	500	25	1.2	1.1999	37 245.5	0.0117	(1,1)
				1.3325	37 246.0	0.0163	(1,1)
b	500	25	1.4	1.7187	37 816.0	0.0290	(1,1)
				1.9441	38 817.2	0.0345	(1,1)
c	500	25	2	3.6595	39 427.4	0.0678	(1,1)
d	500	25	3	9.3638	41 337.5	0.6507	(1,1)
e	500	25	4	9.6879	41 493.9	0.9835	(1,1)
f	5000	30	1.2	4.5722	863 299	0.0179	(2,2)
				7.2395	863 554	0.0608	(2,2)
g	5000	30	1.3	5.8071	873 039	0.0219	(2,2)
				10.191	873 331	0.0996	(2,2)
h	5000	30	1.6	36.125	900 706	0.2781	(3,3)
i	5000	30	1.8	41.850	913 258	0.6588	(3,3)
j	5000	30	3	46.096	923 252	0.9944	(3,3)

where s_{\max} is the number of spin components. The wave function can be used to construct the Lagrangian density:

$$\mathcal{L} = \frac{i\hbar}{2} \Psi^\dagger \frac{\partial \Psi}{\partial t} - \frac{i\hbar}{2} \left(\frac{\partial \Psi^\dagger}{\partial t} \right) \Psi - \frac{\hbar^2}{2m} \sum_{i=1}^N \nabla_i \Psi^\dagger \nabla_i \Psi - \sum_{i=1}^N \Psi^\dagger V_{\text{ext}}(\mathbf{r}_i) \Psi - \sum_{i < j} \Psi^\dagger V_{\text{int}}(\mathbf{r}_i - \mathbf{r}_j) \Psi. \quad (\text{B4})$$

Then one can build the Lagrangian

$$L = \int \mathcal{L} d\mathbf{r}_1 d\mathbf{r}_2 \cdots d\mathbf{r}_N, \quad (\text{B5})$$

and finally the action

$$S = \int_{t_1}^{t_2} L dt. \quad (\text{B6})$$

The principle of stationary action reads

$$0 = \delta S = \sum_i \left[\frac{\partial S}{\partial \varphi_i^*(s_j, \mathbf{r}_j, t)} \delta \varphi_i^*(s_j, \mathbf{r}_j, t) + \frac{\partial S}{\partial \varphi_i(s_j, \mathbf{r}_j, t)} \delta \varphi_i(s_j, \mathbf{r}_j, t) \right]. \quad (\text{B7})$$

The variations over $\varphi_i^*(s_j, \mathbf{r}_j, t)$ and $\varphi_i(s_j, \mathbf{r}_j, t)$ are independent. Taking the variation over $\varphi_i^*(s_j, \mathbf{r}_j, t)$, one gets the Euler-Lagrange equation for $\varphi_i(s_j, \mathbf{r}_j, t)$. Here the Euler-Lagrange equations are called the Hartree-Fock equations and are the following:

$$i\hbar \frac{\partial}{\partial t} \varphi_i(s, \mathbf{r}, t) = \left[-\frac{\hbar^2}{2m} \nabla^2 + V_{\text{ext}}(\mathbf{r}) \right] \varphi_i(s, \mathbf{r}, t) + \sum_{k=1}^N \sum_{s'=1}^{s_{\max}} \int d^3 r' [\varphi_i(s, \mathbf{r}, t) V_{\text{int}}(\mathbf{r} - \mathbf{r}') \times \varphi_k^*(s', \mathbf{r}', t) \varphi_k(s', \mathbf{r}', t) - \varphi_k(s, \mathbf{r}, t) V_{\text{int}}(\mathbf{r} - \mathbf{r}') \varphi_k^*(s', \mathbf{r}', t) \varphi_i(s', \mathbf{r}', t)]. \quad (\text{B8})$$

In our case $s = 1, 2$ or \uparrow, \downarrow . Then we assume that

$$\begin{bmatrix} \varphi_i(1, \mathbf{r}, t) \\ \varphi_i(2, \mathbf{r}, t) \end{bmatrix} \equiv \begin{bmatrix} \varphi_i^{(1)}(\mathbf{r}, t) \\ 0 \end{bmatrix} \quad (\text{B9})$$

for $i = 1, \dots, N/2$ and

$$\begin{bmatrix} \varphi_i(1, \mathbf{r}, t) \\ \varphi_i(2, \mathbf{r}, t) \end{bmatrix} \equiv \begin{bmatrix} 0 \\ \varphi_j^{(2)}(\mathbf{r}, t) \end{bmatrix} \quad (\text{B10})$$

for $i = N/2 + 1, \dots, N$ and $j = 1, \dots, N/2$. We consider only low-energy collisions in the $\uparrow\downarrow$ channel:

$$V_{\text{int}}^{\uparrow\downarrow}(\mathbf{r} - \mathbf{r}') = g \delta(\mathbf{r} - \mathbf{r}'). \quad (\text{B11})$$

Collisions in $\uparrow\uparrow$ and $\downarrow\downarrow$ channels are forbidden:

$$V_{\text{int}}^{\uparrow\uparrow}(\mathbf{r} - \mathbf{r}') = V_{\text{int}}^{\downarrow\downarrow}(\mathbf{r} - \mathbf{r}') = 0. \quad (\text{B12})$$

Finally, one obtains the following equations of motion:

$$i\hbar \frac{\partial}{\partial t} \varphi_i^{(s)}(\mathbf{r}, t) = \left[-\frac{\hbar^2}{2m} \nabla^2 + V_{\text{ext}}(\mathbf{r}, t) + \frac{\delta E_{\text{int}}[\mathbf{n}]}{\delta n_s(\mathbf{r}, t)} \right] \varphi_i^{(s)}(\mathbf{r}, t). \quad (\text{B13})$$

APPENDIX C: DETAILS OF FIGURES

Tables I–III contain the details of Figs. 1, 3, and 4.

TABLE III. Details for the density plots in Figs. 4(a)–4(e).

Panel	λ	Method	$\max_r n_1(\mathbf{r}) - n_2(\mathbf{r}) $	E	\mathcal{P}	(l_1, l_2)
a	3	DPFT	4.3868	1039.752	0.4630	(3,3)
		HF	1.0436	1022.84	0.0983	—
b	4	DPFT	3.9943	1154.929	0.6109	(3,3)
		HF	3.1287	1140.14	0.2008	—
c	7	DPFT	3.2480	1424.63	0.7200	(1,1)
		HF	3.0663	1411.58	0.5317	—
d	10	DPFT	3.0962	1637.30	0.9255	(1,1)
		HF	3.0997	1628.16	0.9332	—
e	15	DPFT	2.4198	1931.07	0.9463	(1,1)
		HF	2.4210	1920.94	0.9565	—

- [1] I. Bloch, J. Dalibard, and W. Zwerger, *Rev. Mod. Phys.* **80**, 885 (2008).
- [2] M. Lewenstein, A. Sanpera, and V. Ahufinger, *Ultracold Atoms in Optical Lattices* (Oxford University, Cambridge, England, 2012).
- [3] I. Boettcher, L. Bayha, D. Kedar, P. A. Murthy, M. Neidig, M. G. Ries, A. N. Wenz, G. Zürn, S. Jochim, and T. Enss, *Phys. Rev. Lett.* **116**, 045303 (2016).
- [4] M. Holten, L. Bayha, A. C. Klein, P. A. Murthy, P. M. Preiss, and S. Jochim, *Phys. Rev. Lett.* **121**, 120401 (2018).
- [5] U. Toniolo, B. C. Mulkerin, X.-J. Liu, and H. Hu, *Phys. Rev. A* **97**, 063622 (2018).
- [6] S. Tung, G. Lamporesi, D. Lobser, L. Xia, and E. A. Cornell, *Phys. Rev. Lett.* **105**, 230408 (2010).
- [7] T. Plisson, B. Allard, M. Holzmann, G. Salomon, A. Aspect, P. Bouyer, and T. Bourdel, *Phys. Rev. A* **84**, 061606(R) (2011).
- [8] M. G. Ries, A. N. Wenz, G. Zürn, L. Bayha, I. Boettcher, D. Kedar, P. A. Murthy, M. Neidig, T. Lompe, and S. Jochim, *Phys. Rev. Lett.* **114**, 230401 (2015).
- [9] K. Fenech, P. Dyke, T. Pepler, M. G. Lingham, S. Hoinka, H. Hu, and C. J. Vale, *Phys. Rev. Lett.* **116**, 045302 (2016).
- [10] P. A. Murthy, M. Neidig, R. Klemt, L. Bayha, I. Boettcher, T. Enss, M. Holten, G. Zürn, P. M. Preiss, and S. Jochim, *Science* **359**, 452 (2018).
- [11] P. Dyke, E. D. Kuhnle, S. Whitlock, H. Hu, M. Mark, S. Hoinka, M. Lingham, P. Hannaford, and C. J. Vale, *Phys. Rev. Lett.* **106**, 105304 (2011).
- [12] A. T. Sommer, L. W. Cheuk, M. J. H. Ku, W. S. Bakr, and M. W. Zwierlein, *Phys. Rev. Lett.* **108**, 045302 (2012).
- [13] C. Cheng, J. Kangara, I. Arakelyan, and J. E. Thomas, *Phys. Rev. A* **94**, 031606(R) (2016).
- [14] T. Pepler, P. Dyke, M. Zamorano, I. Herrera, S. Hoinka, and C. J. Vale, *Phys. Rev. Lett.* **121**, 120402 (2018).
- [15] H. Gong, H. Liu, B. Jiao, H. Zhang, H. Yu, Q. Peng, S. Peng, T. Shu, Y. Zhu, J. Li, and L. Luo, *Phys. Rev. A* **107**, 053321 (2023).
- [16] Y. Guo, H. Yao, S. Dhar, L. Pizzino, M. Horvath, T. Giamarchi, M. Landini, and H.-C. Nägerl, *Sci. Adv.* **10**, eadk6870 (2024).
- [17] Y. Guo, H. Yao, S. Ramanjanappa, S. Dhar, M. Horvath, L. Pizzino, T. Giamarchi, M. Landini, and H.-C. Nägerl, *Nat. Phys.* **20**, 934 (2024).
- [18] J. Schneider and H. Wallis, *Phys. Rev. A* **57**, 1253 (1998).
- [19] P. Vignolo and A. Minguzzi, *Phys. Rev. A* **67**, 053601 (2003).
- [20] E. J. Mueller, *Phys. Rev. Lett.* **93**, 190404 (2004).
- [21] K. Kumagai, M. Saitoh, T. Oyaizu, Y. Furukawa, S. Takashima, M. Nohara, H. Takagi, and Y. Matsuda, *Phys. Rev. Lett.* **97**, 227002 (2006).
- [22] L. P. Pitaevskii and A. Rosch, *Phys. Rev. A* **55**, R853(R) (1997).
- [23] M. Olshanii, H. Perrin, and V. Lorent, *Phys. Rev. Lett.* **105**, 095302 (2010).
- [24] E. Taylor and M. Randeria, *Phys. Rev. Lett.* **109**, 135301 (2012).
- [25] J. Hofmann, *Phys. Rev. Lett.* **108**, 185303 (2012).
- [26] C. Gao and Z. Yu, *Phys. Rev. A* **86**, 043609 (2012).
- [27] C. Chafin and T. Schäfer, *Phys. Rev. A* **88**, 043636 (2013).
- [28] H. Hu, B. C. Mulkerin, U. Toniolo, L. He, and X.-J. Liu, *Phys. Rev. Lett.* **122**, 070401 (2019).
- [29] P. A. Murthy, N. Defenu, L. Bayha, M. Holten, P. M. Preiss, T. Enss, and S. Jochim, *Science* **365**, 268 (2019).
- [30] S. Tsuchiya, R. Watanabe, and Y. Ohashi, *Phys. Rev. A* **80**, 033613 (2009).
- [31] J. P. Gaebler, J. T. Stewart, T. E. Drake, D. S. Jin, A. Perali, P. Pieri, and G. C. Strinati, *Nat. Phys.* **6**, 569 (2010).
- [32] A. Richie-Halford, J. E. Drut, and A. Bulgac, *Phys. Rev. Lett.* **125**, 060403 (2020).
- [33] A. Ptok, *J. Phys.: Condens. Matter* **29**, 475901 (2017).
- [34] U. Toniolo, B. C. Mulkerin, C. J. Vale, X.-J. Liu, and H. Hu, *Phys. Rev. A* **96**, 041604(R) (2017).
- [35] K. Adachi and R. Ikeda, *Phys. Rev. B* **98**, 184502 (2018).
- [36] B. M. Faigle-Cedzich, J. M. Pawłowski, and C. Wetterich, *Phys. Rev. A* **103**, 033320 (2021).
- [37] Q. Zheng, Y. Wang, L. Liang, Q. Huang, S. Wang, W. Xiong, X. Zhou, W. Chen, X. Chen, and J. Hu, *Phys. Rev. Res.* **5**, 013136 (2023).
- [38] C. Stoner, *Proc. R. Soc. London, Ser. A* **165**, 372 (1938).
- [39] T. Sogo and H. Yabu, *Phys. Rev. A* **66**, 043611 (2002).
- [40] T. Karpiuk, M. Brewczyk, and K. Rzążewski, *Phys. Rev. A* **69**, 043603 (2004).
- [41] R. A. Duine and A. H. MacDonald, *Phys. Rev. Lett.* **95**, 230403 (2005).
- [42] L. J. LeBlanc, J. H. Thywissen, A. A. Burkov, and A. Paramekanti, *Phys. Rev. A* **80**, 013607 (2009).
- [43] G. J. Conduit, A. G. Green, and B. D. Simons, *Phys. Rev. Lett.* **103**, 207201 (2009).
- [44] X. Cui and H. Zhai, *Phys. Rev. A* **81**, 041602(R) (2010).
- [45] S. Pilati, G. Bertaina, S. Giorgini, and M. Troyer, *Phys. Rev. Lett.* **105**, 030405 (2010).
- [46] S.-Y. Chang, M. Randeria, and N. Trivedi, *Proc. Natl. Acad. Sci. USA* **108**, 51 (2011).
- [47] D. Pekker, M. Babadi, R. Sensarma, N. Zinner, L. Pollet, M. W. Zwierlein, and E. Demler, *Phys. Rev. Lett.* **106**, 050402 (2011).
- [48] P. Massignan and G. M. Bruun, *Eur. Phys. J. D* **65**, 83 (2011).
- [49] P. Massignan, M. Zaccanti, and G. M. Bruun, *Rep. Prog. Phys.* **77**, 034401 (2014).
- [50] J. Levinsen and M. M. Parish, *Annual Review of Cold Atoms and Molecules* (World Scientific, Singapore, 2015), pp. 1–75.
- [51] M.-I. Trappe, P. Grochowski, M. Brewczyk, and K. Rzążewski, *Phys. Rev. A* **93**, 023612 (2016).
- [52] T. Miyakawa, S. Nakamura, and H. Yabu, *J. Phys. Soc. Jpn.* **86**, 035004 (2017).
- [53] P. T. Grochowski, T. Karpiuk, M. Brewczyk, and K. Rzążewski, *Phys. Rev. Lett.* **119**, 215303 (2017).
- [54] G. M. Koutentakis, S. I. Mistakidis, and P. Schmelcher, *New J. Phys.* **21**, 053005 (2019).
- [55] J. Ryszkiewicz, M. Brewczyk, and T. Karpiuk, *Phys. Rev. A* **101**, 013618 (2020).
- [56] T. Karpiuk, P. T. Grochowski, M. Brewczyk, and K. Rzążewski, *SciPost Phys.* **8**, 066 (2020).
- [57] P. T. Grochowski, T. Karpiuk, M. Brewczyk, and K. Rzążewski, *Phys. Rev. Res.* **2**, 013119 (2020).
- [58] G. M. Koutentakis, S. I. Mistakidis, and P. Schmelcher, *New J. Phys.* **22**, 063058 (2020).
- [59] M.-I. Trappe, P. T. Grochowski, J. H. Hue, T. Karpiuk, and K. Rzążewski, *New J. Phys.* **23**, 103042 (2021).
- [60] J. Ryszkiewicz, M. Brewczyk, and T. Karpiuk, *Phys. Rev. A* **105**, 023315 (2022).

- [61] A. Syrwid, M. Łebek, P. T. Grochowski, and K. Rzażewski, *Phys. Rev. A* **105**, 013314 (2022).
- [62] M. Łebek, A. Syrwid, P. T. Grochowski, and K. Rzażewski, *Phys. Rev. A* **105**, L011303 (2022).
- [63] B. DeMarco and D. S. Jin, *Phys. Rev. Lett.* **88**, 040405 (2002).
- [64] X. Du, L. Luo, B. Clancy, and J. E. Thomas, *Phys. Rev. Lett.* **101**, 150401 (2008).
- [65] G.-B. Jo, Y.-R. Lee, J.-H. Choi, C. A. Christensen, T. H. Kim, J. H. Thywissen, D. E. Pritchard, and W. Ketterle, *Science* **325**, 1521 (2009).
- [66] A. Sommer, M. Ku, G. Roati, and M. W. Zwierlein, *Nature (London)* **472**, 201 (2011).
- [67] C. Sanner, E. J. Su, W. Huang, A. Keshet, J. Gillen, and W. Ketterle, *Phys. Rev. Lett.* **108**, 240404 (2012).
- [68] Y.-R. Lee, M.-S. Heo, J.-H. Choi, T. T. Wang, C. A. Christensen, T. M. Rvachov, and W. Ketterle, *Phys. Rev. A* **85**, 063615 (2012).
- [69] G. Valtolina, F. Scazza, A. Amico, A. Burchianti, A. Recati, T. Enss, M. Inguscio, M. Zaccanti, and G. Roati, *Nat. Phys.* **13**, 704 (2017).
- [70] A. Amico, F. Scazza, G. Valtolina, P. E. S. Tavares, W. Ketterle, M. Inguscio, G. Roati, and M. Zaccanti, *Phys. Rev. Lett.* **121**, 253602 (2018).
- [71] F. Scazza, G. Valtolina, A. Amico, P. E. S. Tavares, M. Inguscio, W. Ketterle, G. Roati, and M. Zaccanti, *Phys. Rev. A* **101**, 013603 (2020).
- [72] H. S. Adlong, W. E. Liu, F. Scazza, M. Zaccanti, N. D. Oppong, S. Fölling, M. M. Parish, and J. Levinsen, *Phys. Rev. Lett.* **125**, 133401 (2020).
- [73] Y. Ji, G. L. Schumacher, G. G. T. Assumpção, J. Chen, J. T. Mäkinen, F. J. Vivanco, and N. Navon, *Phys. Rev. Lett.* **129**, 203402 (2022).
- [74] R. S. Lous, I. Fritsche, M. Jag, F. Lehmann, E. Kirilov, B. Huang, and R. Grimm, *Phys. Rev. Lett.* **120**, 243403 (2018).
- [75] B. Huang, I. Fritsche, R. S. Lous, C. Baroni, J. T. M. Walraven, E. Kirilov, and R. Grimm, *Phys. Rev. A* **99**, 041602(R) (2019).
- [76] P. T. Grochowski, T. Karpiuk, M. Brewczyk, and K. Rzażewski, *Phys. Rev. Lett.* **125**, 103401 (2020).
- [77] B. G. Englert and J. Schwinger, *Phys. Rev. A* **26**, 2322 (1982).
- [78] B. G. Englert and J. Schwinger, *Phys. Rev. A* **29**, 2331 (1984).
- [79] B. G. Englert and J. Schwinger, *Phys. Rev. A* **32**, 47 (1985).
- [80] B.-G. Englert, *Lecture Notes in Physics: Semiclassical Theory of Atoms* (Springer, Berlin, 1988).
- [81] B. G. Englert, *Phys. Rev. A* **45**, 127 (1992).
- [82] M.-I. Trappe, Y. L. Len, H. K. Ng, C. A. Müller, and B.-G. Englert, *Phys. Rev. A* **93**, 042510 (2016).
- [83] M.-I. Trappe, Y. L. L. Len, H. K. K. Ng, and B. G. Englert, *Ann. Phys.* **385**, 136 (2017).
- [84] T. T. Chau, J. H. Hue, M.-I. Trappe, and B. G. Englert, *New J. Phys.* **20**, 073003 (2018).
- [85] B.-G. Englert, in *Proceedings of the Julian Schwinger Centennial Conference*, edited by B.-G. Englert (World Scientific, Singapore, 2019), Chap. 17, pp. 261–269.
- [86] F. Ancilotto, *Phys. Rev. A* **92**, 061602(R) (2015).
- [87] A. K. Das and A. Banerjee, *Eur. Phys. J. D* **72**, 111 (2018).
- [88] P. N. Ma, S. Pilati, M. Troyer, and X. Dai, *Nat. Phys.* **8**, 601 (2012).
- [89] B. P. van Zyl, E. Zaremba, and P. Pisarski, *Phys. Rev. A* **87**, 043614 (2013).
- [90] R. Gangwar, A. Banerjee, and A. Das, *J. Phys. B* **53**, 035301 (2020).
- [91] J. G. Vilhena, E. Räsänen, M. A. Marques, and S. Pittalis, *J. Chem. Theory Comput.* **10**, 1837 (2014).
- [92] M.-I. Trappe, D. Y. H. Ho, and S. Adam, *Phys. Rev. B* **99**, 235415 (2019).
- [93] M.-I. Trappe, J. H. Hue, and B.-G. Englert, in *Density Functionals for Many-Particle Systems: Mathematical Theory and Physical Applications of Effective Equations*, edited by B.-G. Englert, H. Siedentop, and M.-I. Trappe, Lecture Notes Series, IMS (World Scientific, Singapore, 2023), pp. 251–267.
- [94] B.-G. Englert, J. H. Hue, Z. C. Huang, M. M. Paraniak, and M.-I. Trappe, in *Density Functionals for Many-Particle Systems: Mathematical Theory and Physical Applications of Effective Equations*, edited by B.-G. Englert, H. Siedentop, and M.-I. Trappe, Lecture Notes Series, IMS (World Scientific, Singapore, 2023), pp. 287–308.
- [95] M.-I. Trappe and R. A. Chisholm, *Nat. Commun.* **14**, 1089 (2023).
- [96] M.-I. Trappe, W. C. Witt, and S. Manzhos, *Phys. Rev. A* **108**, 062802 (2023).
- [97] M. Aichinger and E. Krotscheck, *Comput. Mater. Sci.* **34**, 188 (2005).
- [98] P. Bloom, *Phys. Rev. B* **12**, 125 (1975).
- [99] L. He, *Phys. Rev. A* **90**, 053633 (2014).
- [100] G. J. Conduit, *Phys. Rev. A* **82**, 043604 (2010).
- [101] G. J. Conduit, *Phys. Rev. B* **87**, 184414 (2013).
- [102] G. Bertaina, *Eur. Phys. J. Spec. Top.* **217**, 153 (2013).
- [103] T. M. Whitehead, L. M. Schonenberg, N. Kongsuwan, R. J. Needs, and G. J. Conduit, *Phys. Rev. A* **93**, 042702 (2016).
- [104] S. Pilati, G. Orso, and G. Bertaina, *Phys. Rev. A* **103**, 063314 (2021).
- [105] H. Heiselberg, *Phys. Rev. A* **83**, 053635 (2011).
- [106] L. He and X.-G. Huang, *Phys. Rev. A* **85**, 043624 (2012).
- [107] L. He, X.-J. Liu, X.-G. Huang, and H. Hu, *Phys. Rev. A* **93**, 063629 (2016).
- [108] R. Schmidt, T. Enss, V. Pietilä, and E. Demler, *Phys. Rev. A* **85**, 021602(R) (2012).
- [109] V. Ngampruetikorn, J. Levinsen, and M. M. Parish, *Europhys. Lett.* **98**, 30005 (2012).
- [110] E. Haller, M. J. Mark, R. Hart, J. G. Danzl, L. Reichsöllner, V. Melezhik, P. Schmelcher, and H.-C. Nägerl, *Phys. Rev. Lett.* **104**, 153203 (2010).
- [111] P. Massignan, Z. Yu, and G. M. Bruun, *Phys. Rev. Lett.* **110**, 230401 (2013).
- [112] H. Tajima and S. Uchino, *New J. Phys.* **20**, 073048 (2018).
- [113] C.-H. Huang and M. A. Cazalilla, *New J. Phys.* **25**, 063005 (2023).
- [114] X.-J. Feng and L. Yin, *Chin. Phys. B* **29**, 110306 (2020).
- [115] W. Ong, C. Cheng, I. Arakelyan, and J. E. Thomas, *Phys. Rev. Lett.* **114**, 110403 (2015).
- [116] B. Fröhlich, M. Feld, E. Vogt, M. Koschorreck, W. Zwerger, and M. Köhl, *Phys. Rev. Lett.* **106**, 105301 (2011).
- [117] C. Kohstall, M. Zaccanti, M. Jag, A. Trenkwalder, P. Massignan, G. M. Bruun, F. Schreck, and R. Grimm, *Nature (London)* **485**, 615 (2012).
- [118] M. Koschorreck, D. Pertot, E. Vogt, B. Fröhlich, M. Feld, and M. Köhl, *Nature (London)* **485**, 619 (2012).

- [119] A. Ciamei, S. Finelli, A. Cosco, M. Inguscio, A. Trenkwalder, and M. Zaccanti, *Phys. Rev. A* **106**, 053318 (2022).
- [120] N. Darkwah Oppong, L. Riegger, O. Bettermann, M. Höfer, J. Levinsen, M. M. Parish, I. Bloch, and S. Fölling, *Phys. Rev. Lett.* **122**, 193604 (2019).
- [121] C. Ravensbergen, E. Soave, V. Corre, M. Kreyer, B. Huang, E. Kirilov, and R. Grimm, *Phys. Rev. Lett.* **124**, 203402 (2020).
- [122] J. von Milczewski, F. Rose, and R. Schmidt, *Phys. Rev. A* **105**, 013317 (2022).
- [123] J. D'Alberto, L. Cardarelli, D. E. Galli, G. Bertaina, and P. Pieri, *Phys. Rev. A* **109**, 053302 (2024).
- [124] B. J. DeSalvo, K. Patel, G. Cai, and C. Chin, *Nature (London)* **568**, 61 (2019).
- [125] J. P. Perdew, A. Ruzsinszky, J. Sun, N. K. Nepal, and A. D. Kaplan, *Proc. Natl. Acad. Sci. USA* **118**, e2017850118 (2021).